Effects of asymmetrical inflow in forward flight on the deformation of interacting flapping wings

Heitzig, Dorian; van Oudheusden, Bas; Olejnik, Diana; Karasek, Matej

Publication date
2019

Document Version
Final published version

Published in
International Micro Air Vehicle Competition and Conference

Citation (APA)
Heitzig, D., van Oudheusden, B., Olejnik, D., & Karasek, M. (2019). Effects of asymmetrical inflow in forward flight on the deformation of interacting flapping wings. In *International Micro Air Vehicle Competition and Conference*

Effects of asymmetrical inflow in forward flight on the deformation of interacting flapping wings

D. N. W. M. Heitzig[*], B. W. van Oudheusden, D. Olejnik, and M. Karásek
Department of Aerospace Engineering, Delft University of Technology, Kluyverweg 1, 2629 HS Delft, the Netherlands

ABSTRACT

This study investigates the wing deformation of a flapping-wing micro air vehicle (MAV) in climbing and forward flight conditions. A measurement setup was developed that maintains adequate viewing axes of the wings for all pitch angles. Recordings of a high-speed camera pair are processed using a point tracking algorithm, allowing 136 points per wing to be measured simultaneously with an estimated accuracy of $0.25\,\mathrm{mm}$. Results of the climbing flight study show that although inflow is symmetric, the wing deformations are slightly asymmetric. Furthermore, it was found that an air-buffer remains present between the wing surfaces at all times, especially with increased freestream velocity. Apart from a minor camber reduction, the clap-and-peel motion remains mostly unchanged for changing velocities, while during the remaining cycle the incidence angle and camber ratio are reduced, together with the angle of attack. In forward flight the clap-and-peel motion is twisted around its contact area to align with the inflow direction, while the general deformation remains unchanged, suggesting similar effectiveness as in hover. Positive mean incidence angles are present for the entire cycle, especially for fast forward flight and stroke reversals. Furthermore, camber is positive during downstroke, while approaching zero for the upstroke in fast forward flight, which suggests low loading during the upstroke.

1 INTRODUCTION

Aerodynamic efficiency of flapping wing fliers was poorly understood until the later part of the 20th century. The low Reynolds number regime in which insects fly should not allow for sufficient lift production to fly. Nonetheless, relatively high lift coefficients are found for hovering insects [1]. Reason for this was later found to be the appearance of strong leading edge vortices (LEV), which remain attached to the wing surfaces and delay stall. Especially the 'clap-and-fling' mechanism was found to harness this effect strongly [2], where LEV are created between two separating wings. The wings were thereby assumed to separate rigidly, without any deformation. Subsequent studies however showed that insect wings are highly flexible, which further increases efficiency due to passive deformations of the wing shape such as dynamic camber production and wing twisting [3]. Camber production is thereby assumed to be especially influential, as it delays the LEV detachments, which improves the delayed stall effect [4].

All effects occur due to the interaction of aerodynamic and structural, i.e. inertial and elastic, forces and must therefore be considered in all discussions. Inertial forces acting on the wing trailing edge were for instance found to result in a phase lag [5], which initiates a recoil effect after stroke reversal that is beneficial to thrust production [6]. Elastic forces built up over the stroke can lead to extended rotation of the wing trailing edge at the stroke end, while aerodynamic forces act as damping [7].

In this study, the specific interaction of the flapping wing micro air vehicle (MAV) 'DelFly II' [8], henceforth simply called 'DelFly', is investigated. This MAV features two wing pairs in an X-wing configuration, which 'clap-and-peel' [5] on each side. Several studies of the force production [9] and flowfield around the DelFly have already been carried out [10, 11, 12], however the wing deformation was treated comparatively little [7]. So far, for simplicity the deformation was considered to be purely symmetrical, as only a stationary hover case was studied. This study extends on this work and introduces a freestream velocity in which the DelFly is pitched to different angles, thus simulating forward flight. This problem is especially interesting, as the clap-and-peel deformation was investigated only very little outside its designed symmetrical condition [13] and potentially opposing effects such as asymmetrical camber and incidence angle deformations are seen to come into play as fast forward flight is approached [3, 6].

2 EXPERIMENTAL SETUP

The used DelFly MAV (Figure 1) consists of only the X-wing pair with half span, $s_{tip} = 140\,\mathrm{mm}$, the flapping mechanism enabling stroke angles of $\phi = 44°$, the electronic speed controller and a central airframe to which it is mounted. Similar as in other tethered studies of the DelFly, the tail is omitted, and power is supplied externally using a laboratory power-supply and servo tester to generate the flapping frequency signal. The wing material is chosen to be $15\,\mu\mathrm{m}$ thick

---

[*] Email address: dorian.heitzig@me.com

Mylar, together with the default stiffener setup featuring a D-shaped leading edge rod which increases the stiffness in the stroke plane [8].

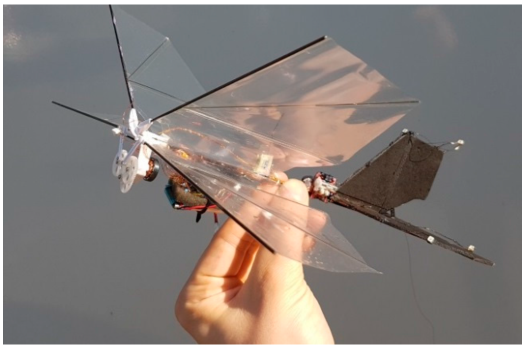

Figure 1: DelFly II MAV. The used model omits the tail and electronics. [11]

Several different optical measurement methods were considered for the measurement of the wing deformation. Ultimately, a back-light point tracking method [7] was chosen, that tracks distinct points placed on the wing over time, thus giving information of the overall wing deformation. Preliminary tests showed that compared to other methods such as digital image correlation [14] or fringe projection [15, 16], this method can be used to measure both wings simultaneously from one stereo view pair as it does not require opaque wings. Instead, the default transparent DelFly wings can be used, which allows points to be captured through an overlying wing. Methods that require opaque wings will either need optical measurement equipment on both sides of the object or separate measurements of the wings which must later be synchronized and aligned, likely increasing the measurement uncertainty.

2.1 Measurement setup

The basis of the measurement setup is formed by a frame, which is mounted on a rotating stage positioned below the center of an open $600\,\mathrm{mm} \times 600\,\mathrm{mm}$ windtunnel test section, as shown in Figure 2. The DelFly is mounted on its side, positioned so that the quarter wing chord is exactly over the rotational axis and at 10° pre-pitch relative to the plane of the frame. This proved to give the best optical access through the flapping cycle by the two cameras which are mounted at $\pm 10^\circ$ relative to the frame. The used cameras are two Photron Fastcam SA 1.1 with a CMOS sensor with a 1024 pixel x 1024 pixel resolution and $20\,\mu\mathrm{m}$ pixel pitch capturing at $2\,\mathrm{kHz}$ and $1/2000\,\mathrm{s}$ exposure. Both are positioned around $600\,\mathrm{mm}$ from the DelFly and are fitted with a Nikon lens with $60\,\mathrm{mm}$ focal length and $f\# = 16$ mounted on a Scheimpflug adapter. The background illumination is provided by three LaVision LED-Flashlight 300 lamps also mounted to the frame. The lamps are pulsed in sync with the cameras with $10\,\%$ duty cycle. Although the lamps produce a relatively large and homogeneous light area, they are further diffused using a combination of a frosted acrylic screen and paper, mounted to the windtunnel nozzle.

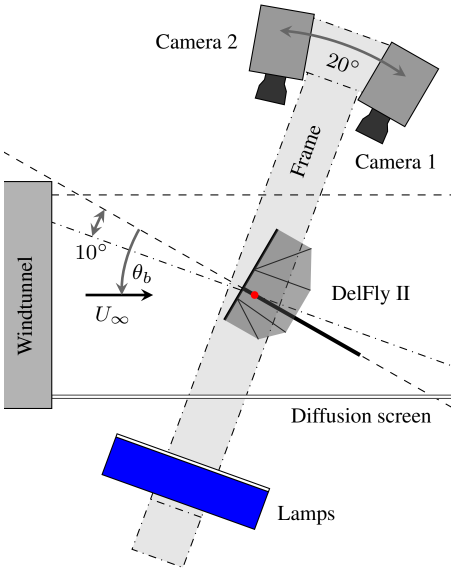

(a) Top-down sketch on the test section with the DelFly pitched with θ_b around the rotation axis (red).

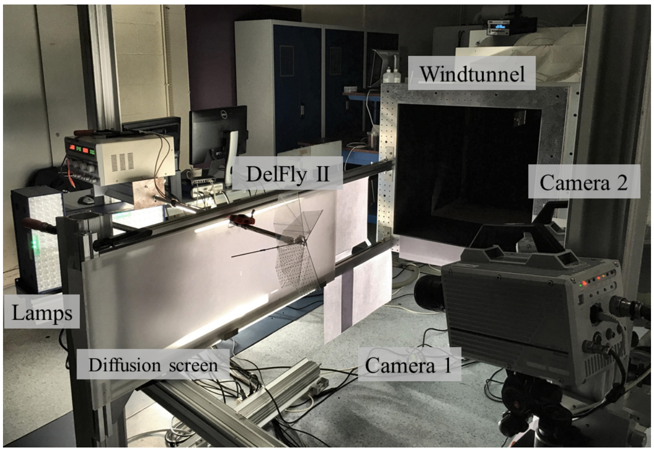

(b) Picture of the measurement setup showing the DelFly mounted in front of the windtunnel nozzle.

Figure 2: Measurement setup.

This setup allows the pitch angle, θ_b of the DelFly to be adjusted from 0° to 70° by simply manipulating the rotating stage. No readjustments of cameras or lamps are needed to maintain good visibility of the wing deformation, which would require frequent re-calibrations. The only exception is that for $\theta_b \geq 50^\circ$ an additional halogen lamp is added on the camera side to provide sufficient illumination of the region close to the windtunnel nozzle where the background illumination no longer reaches.

The points are applied on the wing using a permanent marker as shown in Figure 3. Per wing, a total of 136 black markers of approximately $1\,\mathrm{mm}$ radius spaced at around $7.5\,\mathrm{mm} \times 10\,\mathrm{mm}$ are applied, thereby the grid is shifted between the upper and lower wing, so that overlapping of points during the contact phase is avoided. The marker position is exact to approximately $1\,\mathrm{mm}$, this has however only very little influence on the measurement process and in theory any arbitrary point spacing may be used.

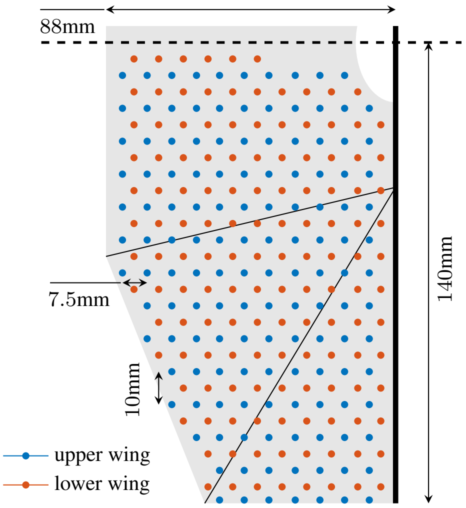

Figure 3: Schematic of DelFly wing half with point grids.

2.2 *Point tracking algorithm*

The recorded images are processed using a point tracking algorithm coded in MATLAB. Essentially, the algorithm uses a temporal tracking method to follow the image point movements, which are then triangulated to obtain the world locations. However, as points are not easily distinguishable, small errors due to for instance minor inaccuracies in the exact point location, can over time lead to larger errors such as snapping of the points to an incorrect one, especially as the path of points of the two wings often cross. Therefore, the known point spacing is used to reduce noise in the predictions and to detect errors. Once a full flapping cycle is measured, these measurements are used as predictions for the following cycles. This allows the algorithm to run fully automated, with only limited initial manual inputs. The following paragraphs explain the algorithm in more detail.

Initially, the images recorded in the LaVision software DaVis are imported into MATLAB and pre-processed, which includes distortion correction, background removal using separately recorded images, image inversion and Gaussian smoothing with a 7×7 kernel size. The camera model necessary for distortion correction and later triangulation was created using the MATLAB stereo camera calibration toolbox.

A two-stage Circular Hough Transform (CHT) method [17] is used to detect the wing points, starting with a recording where the wings are in contact and almost orthogonal to the camera view. One point per wing must be selected manually, the following will then be detected automatically using the known point spacing and an estimated magnification factor. With all points detected in all views, the stereo calibration is used to calculate the world positions.

For the subsequent timesteps, a temporal tracking method is used to predict the point locations. Therefore, an up to third degree polynomial is fitted to the growing time-series, which coefficients can be used to determine the point velocity components (after the first timestep they are assumed to be zero). The velocity vector multiplied by the timestep then gives an estimation of the point pixel shift. As the determined point locations contain some error, noise quickly accumulates in the determined velocities. Therefore, a spatial fit of the velocities is computed using radial basis interpolation using a C^2 compact support function, which is used instead of the calculated velocity if the difference between calculated and fitted velocity is larger than the velocity fit itself. It showed thereby that normalizing the velocities with the span-wise point location, analogous to the rotational velocity around the stroke axis, improves the spatial interpolation.

The true point locations are then determined as the simultaneous correspondence between all point predictions and CHT measurements which minimizes the total prediction error. This simultaneous matching of both wings avoids incorrect correspondence of points which easily occurs when points in close proximity are sequentially corresponded. The optimization is done using a mixed-integer linear programming algorithm, where duplicate use of a measured point is prevented using constraints. If no measurement that fulfills the set tolerance could be found, the point status is set to missing.

These points are neglected in the spatial predictions. Furthermore, in the following timesteps they are corresponded after successfully found points using the world re-projection instead of the temporal prediction. If the point status in one view is considered correct, the prediction is improved further by moving the re-projection onto the epipolar line.

Nonetheless, points correspondences can be incorrect, e.g. due to incorrect detection by the CHT method, or snapping to wrong points due to noise in the tracking. Therefore, a check for incorrect point measurements is also done in the world domain. Here, a spatial fit of the triangulated world points is created using the previously used radial basis interpolation for the in-plane location together with a polynomial fit for the out of plane location. Points which measured location lies more than $2.5\,\mathrm{mm}$ from the fit, or have a reprojection error above 1.5 pixel, are assumed to be incorrectly triangulated.

Once a point exceeds this tolerance by a factor of two, a correction of the triangulation is attempted. Therefore, the view with lower certainty is selected, which is the view where either no point measurement could be corresponded or where the reprojection of the spatial fit lies further from the measured point location. This incorrect point view is then handled like the missing points described above. The increased tolerance of the correction is used to prevent overuse of corrections without allowing incorrect triangulations to be considered in the spatial predictions.

After a full cycle is measured, the exact cycle length is determined which allows to combine the measurement series to a single cycle. This series is then resampled, thereby filling gaps where points could not be found, to create a prediction for the following cycles. This cyclic prediction is improved with each full cycle as new measurements are added.

The complete measurement series is low-pass filtered using a MATLAB function to remove noise. The cut-off frequency was set to the 10th flapping harmonic, i.e. between $100\,\mathrm{Hz}$ and $130\,\mathrm{Hz}$, which is conservative compared to the influence limits found in other studies [18, 19].

The described algorithm works well in determining the DelFly wing deformation. On average, the reprojection error lies at around 0.21 pixel with $3.4\,\%$ point tracks are determined to be incorrect based on the mentioned criteria. The tracking quality is thereby lower for the second cycle half and the lower wing as point motions are possibly less favorable and larger points are more often occluded by stiffeners. Worse tracking results in isolated false positive point measurements, which increase the mean reprojection error.

Measurements of a $150\,\mathrm{mm}$ diameter reference sphere were done to get a better understanding of the general setup accuracy. The 63 markers of $1\,\mathrm{mm}$ radius had an average reprojection error of 0.11 pixel, resulting in an average distance of $0.12\,\mathrm{mm}$ from the fitted sphere surface. Assuming a linear relation with the reprojection error, the deformation measurements can be said to be accurate to approximately $0.25\,\mathrm{mm}$.

3 RESULTS

As forward flight of the DelFly results in simultaneous variation of pitch angle and flapping frequencies together with the inflow velocity, the effects of each parameter by itself should be understood. Previous studies have already addressed the effects of the flapping frequency variations [7]. Studies on the wing deformation due to increasing inflow velocity however have not yet been done, therefore this effect is analyzed before the forward flight results. Climbing flight is of further interest as recent tailless DelFly can sustain such condition more reliably [20].

The following discussion uses the measured points to represent the wing surface, i.e. the most forward and backward point are used as wing leading and trailing edge, respectively. To obtain equivalent parameters, the points on the lower wing are interpolated to match the upper wing. The total of 2000 measurements is allocated to 100 phase bins over the flapping cycle to calculate the deformation statistics. The phase is thereby indicated by the non-dimensionalized time, $t^* = t/T$, where period, $T = 1/f$, with $t^* = 0$ at the closest distance between the wing leading edge. Thus, the cycle starts with the outstroke and ends with the instroke.

The point measurements are transferred from the body coordinate system to a wing coordinate system fixed to the wing leading edge shown in Figure 4a. An exemplary $x_w - z_w$ cut at span location s_w is shown in Figure 4b. In this plot, the shown measurements are normalized by the mean chord, $c_{mean} = 80\,\mathrm{mm}$, indicated by the asterisk and the origin is shifted by $\Delta z_w = tan(\phi)s_w$ to the intersection with the dihedral plane as done in [7] to visualize the stroke angle.

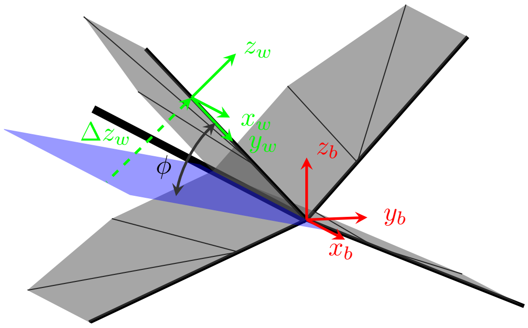

(a) Sketch of the DelFly including body (red) and local wing (green) coordinate systems and dihedral plane (blue).

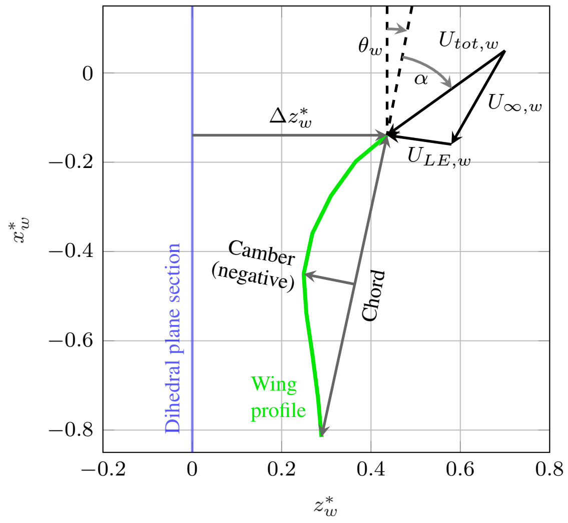

(b) Definition of wing profile parameters in normalized $x_w^* - z_w^*$ plane at spanwise location s_w.

Figure 4: Used coordinate systems.

The wing coordinate system is also used to calculate different local wing profile parameters, later used for a quantitative description of the deformation. The camber ratio, ϵ is the ratio of camber and chord, where a curvature against z_w-direction is defined as negative, as shown. The incidence angle, θ_w is the angle between the chordline and the x_w-axis and used to describe wing twisting. The difference between incidence angle and angle of the inflow velocity, $U_{tot,w}$ is used to represent the angle of attack, α. Thereby the inflow direction is calculated from the sum of the freestream velocity in the wing reference frame, $U_{\infty,w}$ and leading edge velocity, $U_{LE,w}$, however neglects induced velocities.

3.1 Climbing flight

In ideal hover or climb, the DelFly is orientated vertically remaining approximately in a fixed location in the horizontal plane. The vertical force is produced by the flapping wings, while conventionally a tail maintains stability. The frequency required to maintain hover lies above 13 Hz [9, 12] and must increase further to achieve climbing flight. Here, three cases were tested, ranging from hover with zero freestream velocity to $U_\infty = 1\,\mathrm{m\,s^{-1}}$ and $2\,\mathrm{m\,s^{-1}}$ at $\theta_b = 0°$. The flapping frequency was kept constant at 12 Hz, the results are therefore not representative for free flight, as the main objective is to understand the basic effects of non-zero inflow velocity.

A representation of the temporal development of the wing deformation is given in Figure 5. The spanwise location, $s_w = 100\,\mathrm{mm} = 0.71 s_{tip}$ is chosen as it showed to give a good representation of the average wing shape. In spanwise direction the deformation is relatively straightforward where the deformation magnitude typically increases towards the wing tips while maintaining the same temporal trends.

The clap-and-peel phase, where the wings are rolling off on each other can clearly be seen in the figure. The duration is slightly reduced from $\Delta t^* = 0.174$ to 0.193 (based on trailing edge detachment at $s_w = 100\,\mathrm{mm}$) at faster climb speeds. As found by others, the leading edges thereby make no contact [7]. This gap appears larger in hover, and is increased especially towards the root, where a large gap remains for the entire first wing half. However, also for the remaining wing surface, minimal distances were found to remain. Opposed to the wing leading edge, the wing surfaces are closest at the hover case, with distances of around 0.7 mm close to the wing tip. At $U_\infty = 2\,\mathrm{m\,s^{-1}}$ the minimal distance lies around 1.3 mm. The general presence of this 'air-buffer' between the wing surfaces is plausible, as viscous forces prevent large fluid accelerations close to the wing surfaces. Determining an exact reason for this behavior is however difficult, and is likely due to a combination of interactions over the entire wing cycle, such as pressure fields and elastic forces.

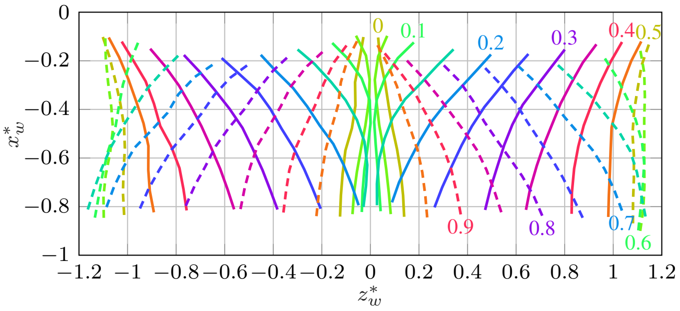

(a) Hover. t^* is indicated for the upper wing.

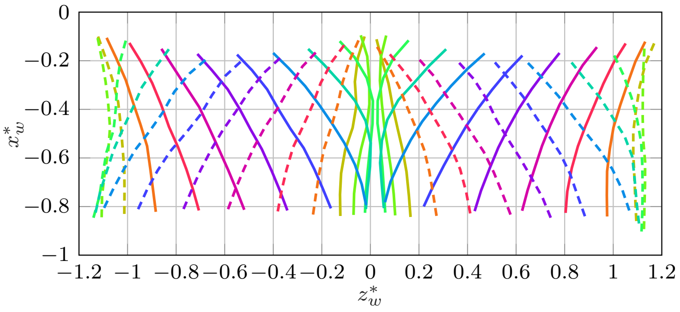

(b) $1\,\mathrm{m\,s^{-1}}$ climb.

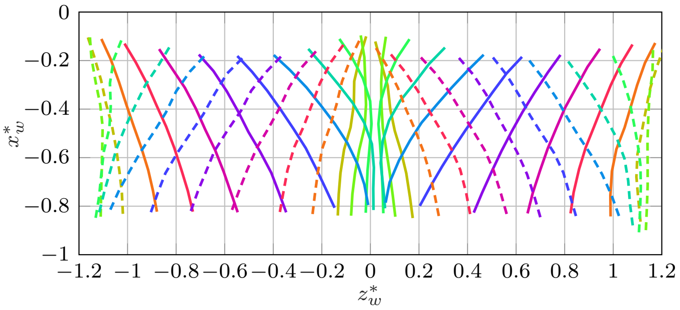

(c) $2\,\mathrm{m\,s^{-1}}$ climb.

Figure 5: Wing profile deformation at $s_w = 100\,\mathrm{mm}$ over the flapping cycle due to different climbing velocities. The upper wing can be seen in the right half, the outstroke profiles are dashed.

Even for this symmetrical inflow case, the wing deformations show clear asymmetries, which has not previously been noted. These asymmetries are visible especially during the end of the outstroke, where the lower wing displays camber while the upper wing is mostly flat. This effect is reduced at higher flow-speeds. Also, the leading edges heave of both wings are clearly asymmetric. The upper wing heaves considerably more during the instroke than during the outstroke, while the lower wing heaves approximately identically during both strokes. Multiple reasons could result in this asymmetry. The dihedral angle of the DelFly already introduces a slight asymmetry, as the upper wings come closer to each other than the lower. This leads to minor differences in the aerodynamic behavior, as well as possible asymmetric wing tensioning. Inaccuracies in the manual manufacturing process of the wings can increase this effect. Further discrepancies may be introduced by the measurement procedure, e.g. the support, the diffusion wall and possibly small uncertainties in the set pitch angle.

A closer investigation is done based on the wing profile parameters shown in Figure 6. Although asymmetries are again evident in the plots, as well as relatively large standard deviations (s.d.) at some instances, trends are still clearly visible and allow a discussion of the results.

Through the clap and peel, the incidence angle changes with an almost equal rate for all cases. The wing in hover is thereby initially twisted least outwards, and therefore twisted most inwards at the end of the clap-and-peel phase.

In the outstroke phase, the wing incidence angle peaks at the time where the trailing edges detach, around $t^* = 0.18$ at this span location. Once detached, the trailing edge velocities become much larger than the leading edge velocities, which starts to reduce the incidence angle. The large acceleration is likely due to the elastic forces build-up during the clap-and-peel phase. The incidence angle of the hover case thereby start to decrease faster than that of the climb cases, which results in lower inwards wing twisting during the last part of the outstroke. Looking at the wing deformation plots, it can be seen that in fact the trailing edge location at the end of the outstroke is similar for all cases, while the leading edge moves further in the stroke plane direction.

This can be explained by the aerodynamic forces, which are dominant during the high stroke velocity phase. Due to the high freestream component for the fast climb case, the inflow angle is quite low, in fact similar to the incidence angle. For $U_\infty = 2\,\mathrm{m\,s^{-1}}$, this results in a low angle of attack of $|\alpha| \approx 20°$ during the majority of the fast stroke phases, as can be seen in Figure 6c. Analysis of the spanwise distribution shows that this holds for most of the wing, only at the wing tip larger angles are found. This alignment of the inner wing surface with the inflow direction results in reduced wing loading, which in turn reduces the damping effect of the aerodynamic forces, thus allows the leading edge to stroke further.

At $U_\infty = 1\,\mathrm{m\,s^{-1}}$, the inflow angles are already considerably larger, resulting in larger angles of attack, and in the hover case even increases to $\alpha \approx 90°$, although the low velocity magnitude makes this phase irrelevant. The large spike in angle of attack around the stroke reversal occur due to small changes in the leading edge movement direction and should therefore also be neglected. Similarly, an incorrectly corresponded point of the hover case at $t^* = 0.42$ results in the downwards α spike.

The instroke then behaves mostly as the outstroke, with the incidence angle of the climb cases again lagging the hover case. The incidence angle increases at an even higher rate, which can be linked to a torsional wave traveling down the wing span [6] seen in the 3D animation (Video 1). The

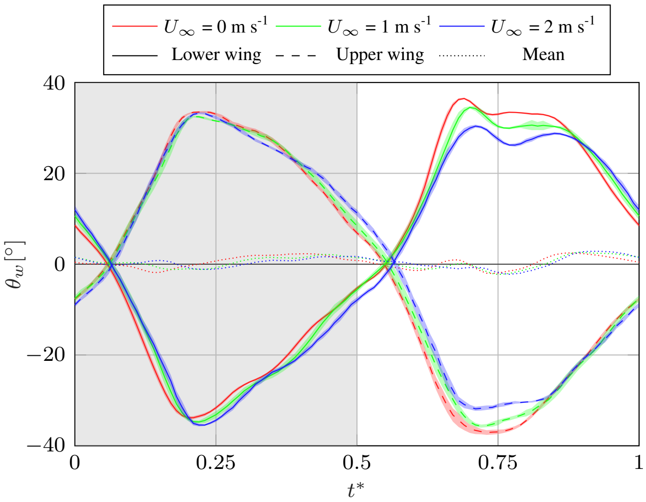

(a) Incidence angle.

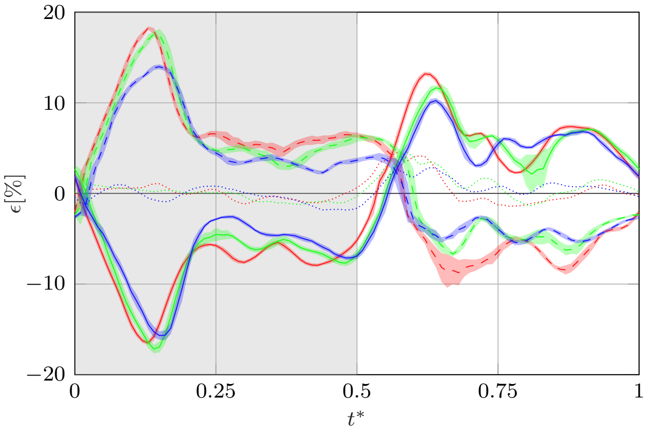

(b) Camber ratio.

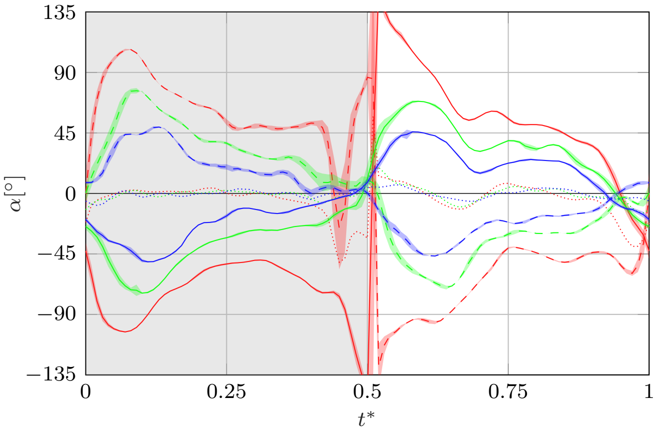

(c) Angle of attack.

Figure 6: Wing profile parameters at $s_w = 100\,\mathrm{mm}$ due to different climbing velocities indicated by U_∞. The outstroke phase is shaded in grey, the instantaneous s.d. is shaded in the respective color.

maximum incidence angle obtained by the hover case now reaches a considerably larger values compared to climbing flight, which can again be attributed to respective inflow direction, which results in low angles of attack and loading during climb. The incidence angle is now maintained for a longer period, where again the angle of the hover case reduces earlier, and the leading edges stop further apart when compared to the climb cases.

Apart from the wing twisting, camber or interchangeably camber ratio also plays a significant role in force production and is worth analyzing. The wing peel leads to a large camber production during the cycle start. On average, the wings of the hover case have thereby slightly larger camber ratios, which appears to be due to the faster detachment of the leading edges and a lower wing surface distance. As for the incidence angle, the maximum camber ratio is reduced quickly once the trailing edges separate. In the following out- and instroke, the camber ratio is lower for the climb cases. This is likely linked to the reduced inflow angle, which is assumed to lead to lower wing loading. At the start of the instroke, the camber shows also a peak, although lower than that during the clap-and-peel of the outstroke. This is similar to the recoil effect seen to increase thrust production in different insects [5, 6], which occurs due to inertial forces leading to trailing edge lag. Outside the clap-and-peel, the camber ratio decreases close to the wing tip, which is against the general spanwise trends and assumed to be due to the stiffener positioning [7]

3.2 Forward flight

During horizontal forward flight, the DelFly is pitched forward, which results a horizontal component of the forces produced by the flapping wings. The pitch angle and flapping frequency must then be matched to maintain horizontal flight at a certain velocity. To simulate this in the windtunnel, the parameters θ_b, f and U_∞ were set to replicate values measured in previous free forward flight investigations [9, 12]. The cases investigated here are shown in Table 1.

θ_b [°]	U_∞ [$\mathrm{m\,s^{-1}}$]	$U_{\infty,z}$ [$\mathrm{m\,s^{-1}}$]	f [Hz]
70	0.50	0.47	13.00
50	1.12	0.85	11.89
40	1.63	1.05	11.07
30	2.26	1.13	10.11

Table 1: Tethered flight settings representing free forward flight.

Changes of the wing deformation are therefore not purely dependent on the changing pitch or inflow direction, but are a result of the combination of the three parameters. Additionally to the terms in- and outstroke, which described the wing movement towards and from the dihedral plane, with the introduced horizontal orientation the terms downstroke and upstroke are now used. These describe the wing movement relative to the horizon, and correspond inversely to in- and outstroke for the upper and lower wing.

The wing profiles at $100\,\mathrm{mm}$ span location presented in Figure 7 show that the introduced asymmetry of inflow direction and force production has a large influence on the wing deformation and goes beyond the minor asymmetries found in the climbing cases. In all cases a mean incidence angle directed towards the inflow direction is present. This effect increases especially for low pitch angles, see for instance the wing contact region and the trailing edge location at the outstroke end. This suggests that the increased freestream velocity during these phases has a larger influence than the pitch angle alone. In fact, the asymmetry appears to be proportional to the freestream component in z_w direction, $U_{\infty,z} = sin(\theta_b) \cdot U_\infty$, listed in Table 1.

Interesting to see is that the core clap-and-peel deformation remains relatively unaffected by the pitch angle and appears to be simply rotated to a twisted wing contact plane. The leading edge path of the lower wing is therefore directed considerably more backwards, which results in an asymmetric heave of both wings, where the wings are heaved more during downstroke. This typically indicates higher loads during this phase, which is in line with the required lift production. The clap-and-peel duration at $s_w = 100\,\mathrm{mm}$ reduces slightly from $\Delta t^* = 0.185$ to 0.165 for faster forward flight.

The wing parameter plots shown in Figure 8 give further insight into the deformations. For all cases, the mean incidence angle is positive over most of the cycle, especially for the cases with large normal freestream component. This trend is especially large during stroke reversal, where the inflow velocity is almost entirely made up by the freestream velocity. Also, the upstroke, where the incidence angle is negative, varies more with the pitch angle.

Little differences in incidence angle during the clap-and-peel phase show again that this phase is relatively unaffected by the asymmetric inflow. Difference is only a shift in the initial incidence angle, while the incidence angle increase rate remains identical. The final angle difference between the wings is in line with the effect of reduced flapping frequency [7].

The assumption that the clap-and-peel behavior is largely unaffected is also supported by the measured camber deformation. While initially the both wings have positive camber ratios, between $t^* = 0.05$ and $t^* = 0.18$ the camber ratio is almost symmetric. The reduced magnitude can again be linked to the reduction in flapping frequency [7] and reduced freestream velocity. The $\theta_b = 50°$ case is the only outlier for

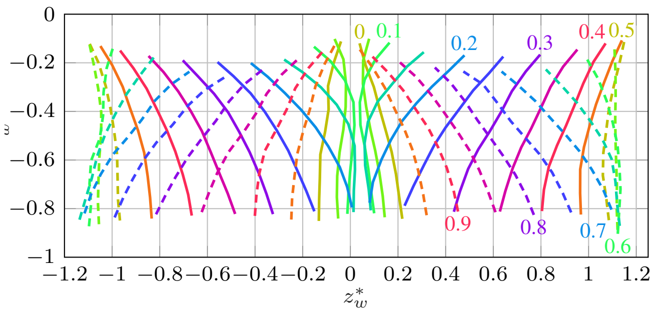

(a) $0.5\,\mathrm{m\,s^{-1}}$ forward flight at $\theta_b = 70°$. t^* is indicated for the upper wing.

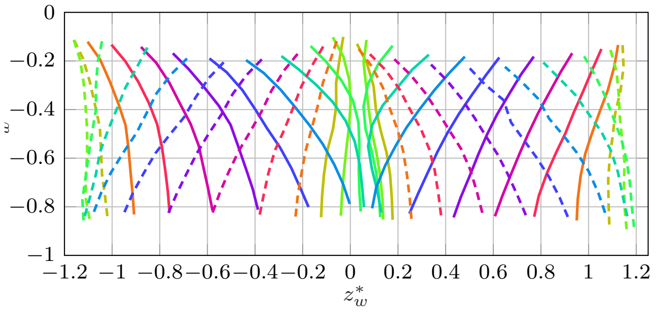

(b) $1.12\,\mathrm{m\,s^{-1}}$ forward flight at $\theta_b = 50°$.

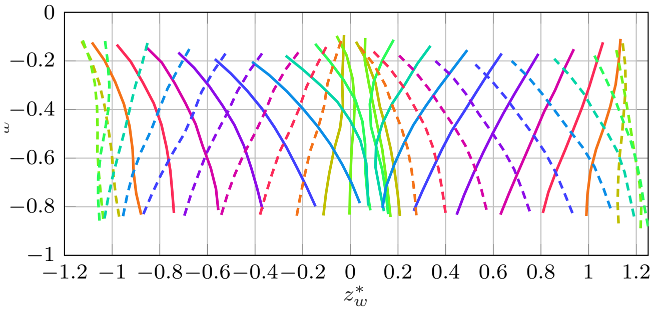

(c) $1.63\,\mathrm{m\,s^{-1}}$ forward flight at $\theta_b = 40°$.

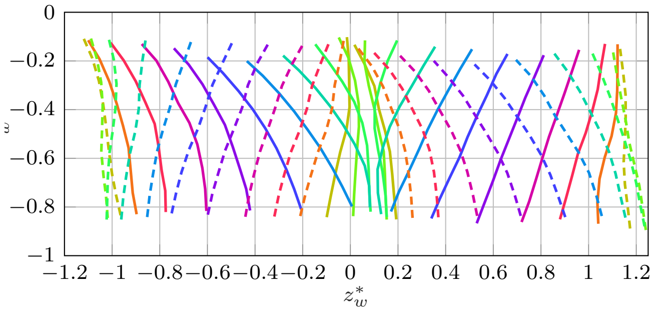

(d) $2.26\,\mathrm{m\,s^{-1}}$ forward flight at $\theta_b = 30°$.

Figure 7: Wing profile deformation at $s_w = 100\,\mathrm{mm}$ over the flapping cycle due to different different forward flight velocities. The upper wing can be seen in the right half, the outstroke profiles are dashed.

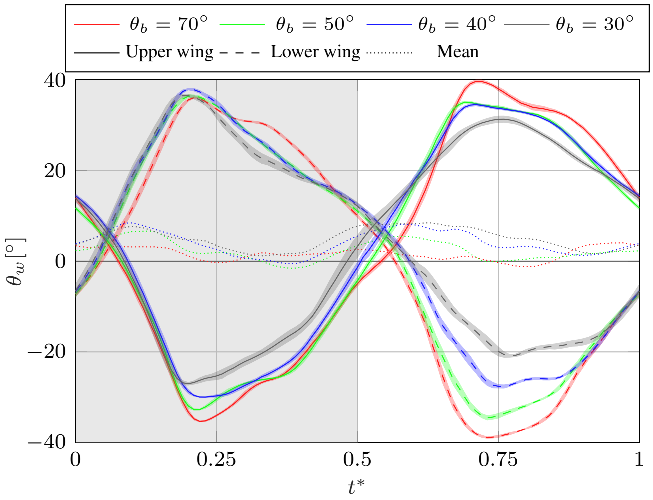

(a) Incidence angle.

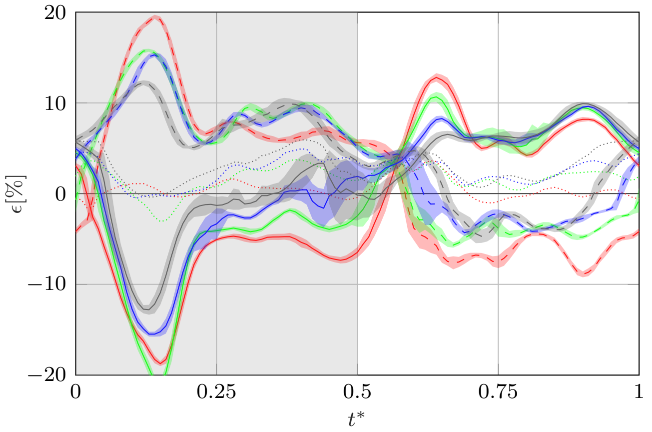

(b) Camber ratio.

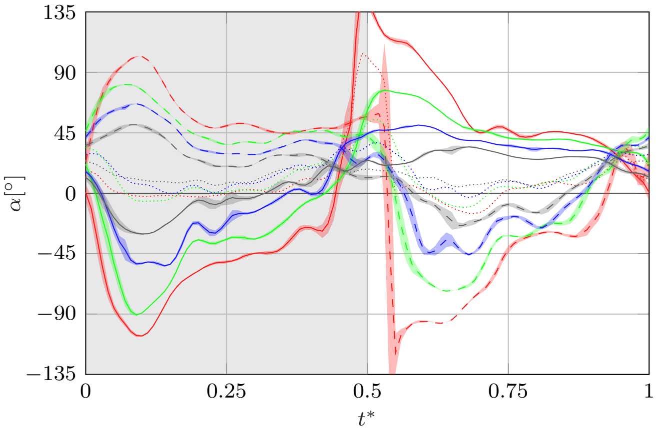

(c) Angle of attack.

Figure 8: Wing profile parameters at $s_w = 100\,\mathrm{mm}$ due to different forward flight velocities indicated by θ_b. The outstroke phase is shaded in grey, the instantaneous s.d. is shaded in the respective color.

this assumption, the camber production during peel follows no clear trend. This appears to be due to the specific contact region rotation, which results in a sharper peel angle in this case.

For the $\theta_b = 70°$ case, the camber deformation is quite similar to the hover case. Larger asymmetries occur for lower pitch angles. Here, during the downstroke similar positive camber ratios occur for all cases, while during the upstroke the camber ratio reduces approximately proportional with the pitch angle, approaching zero for $\theta_b = 30°$, a behavior that is common in insect flight [3, 6]. Figure 7d shows that the upper wing profile has an S-shape towards the end of the outstroke, which makes the determination of the camber direction difficult, thus leads to large s.d.. The wing surface towards the leading edge is thereby already curved upwards, while the trailing edge is still curved downwards. Towards the wing tip this behavior is increased where the entire profile is inverted already before the stroke reversal. This suggests that the wing is here already beginning to produce lift and possibly a LEV starts to develop on the upper wing surface. This effectively moves the start of the lift producing phase of the upper wing forward.

This may be an explanation for the absences of a large initial camber production, previously called recoil, and the reduction of the torsional wave. Recoil remains visible only for $\theta_b = 70°$.

Further links can be drawn between the camber and twist development to the wing loading, represented by the angle of attack. As already seen for the camber development, during the clap-and-peel phase the angle of attack is relatively symmetric, and large angles of attack still indicate the production of LEV even in the fastest forward flight case. This, together with the alignment of the clap-and-peel motion with the flight direction, will likely result in the majority of the required thrust being produced during this phase. This could reduce the need for the wings to produce thrust during upstroke, as it is assumed to occur for single wing fliers [3].

Afterwards, the angle of attack is similar for both stroke halves, where during the downstroke the angle of attack remains mostly constant in time, while reducing considerably for the upstroke. This occurs due to motion of the wings relative to the freestream, which also leads to higher relative velocity of the wing during downstroke [19]. This change in loading directly corresponds to the change in camber, which partially speaks for a well working passive deformation properties of flexible flapping-wings. This can be seen particularly for the $\theta_b \leq 40°$ cases, where $\alpha \approx 0°$ during the last part of the upstroke of both wings. It was assumed that the wings already start producing lift at this span location, and indeed the sign change of α and ε coincide very closely. This is remarkable, especially considering the neglection of induced velocities in α and the likely presence of structural effects.

4 CONCLUSION

Previous studies on the wing deformation of the DelFly in hovering flight [7] were extended to climbing flight of up to $2\,\mathrm{m\,s^{-1}}$ and forward flight with 70° to 30° pitch. An optical measurement setup was developed which co-aligns a camera pair together with the DelFly and the background light to maintain adequate viewing axes of the wings which undergo large stroke angles. As the wings are transparent, 136 points applied to each wing could be measured simultaneously. The points were tracked using an in house developed point tracking algorithm, which uses known structural information to enhance the temporal tracking so that very few false point matches occur. The general accuracy lies around $0.25\,\mathrm{mm}$ based on reference sphere measurements. The developed setup and measurement algorithm may be useful in the future for investigating different flight states or other models and may also be an important tool for optimizing wing designs and generating validation data for numeric methods.

The carried out measurements show different general deformation behaviors of interacting flapping-wings, which to the best of our knowledge have not yet been noted in literature. Firstly, measurements show that the wing surfaces do not touch during the clap-and-peel phase, instead an air-buffer remains at all times. This air-buffer lies between $0.7\,\mathrm{mm}$ and $1.3\,\mathrm{mm}$ and increases with inflow velocity. Furthermore, slight asymmetries are found even in symmetrical inflow conditions. These are assumed to be to an extent inherent because of the dihedral angle which influences aerodynamics and wing tension, but may also be a result of measurement uncertainties.

Apart from this, the climbing flight study showed that the increase in freestream velocity has relatively little effect on the clap-and-peel, only minimal camber reductions were found. The incidence angle is mostly unaffected during the entire outstroke, as elastic energy stored during the clap-and-peel is released during the remaining cycle half. Otherwise, camber ratio and incidence angle are reduced with increasing climbing rate, which is assumed to be driven by lower wing loading, indicated by the angle of attack. Torsional waves traveling in spanwise direction were found, as well as recoil-like camber increase at the cycle start.

The forward flight study showed that asymmetries are especially large in fast forward flight, which suggests that asymmetric deformations are not proportional to pitch angle but to the normal freestream component. Clap-and-peel deformation is thereby again mostly unaffected, indicating that the produced LEV has a dominant effect over the asymmetrical freestream velocity and that the motion likely remains as effective as in hover. Varied is only the motion symmetry plane, which is now twisted to align more with the inflow. A positive mean incidence angle is present during the entire cycle, and especially large during the stroke reversal, where the tip velocities are low. The camber production now differs between up- and downstroke: During the downstroke wings remain cambered upwards, while during the downstroke the negative camber is heavily reduced for fast forward flight. This, together with the angle of attack estimation indicates very low wing loading during upstroke. The calculation of α thereby neglects the presence of large unsteady aerodynamic effects, for instance due to LEV and wing rotation. This makes the estimation of the loads difficult and prevents extended discussion, which may be addressed in future work.

REFERENCES

[1] A. R. Jones and H. Babinsky. Unsteady lift generation on rotating wings at low reynolds numbers. *Journal of Aircraft*, 47(3):1013–1021, 2010.

[2] T. Weis-Fogh. Quick estimates of flight fitness in hovering animals, including novel mechanisms for lift production. *J. Exp. Biol*, 59:169–230, 1973.

[3] H. Wang. Measuring wing kinematics, flight trajectory and body attitude during forward flight and turning maneuvers in dragonflies. *Journal of Aircraft*, 206(4):745–757, 2003.

[4] G. Du and M. Sun. Effects of unsteady deformation of flapping wing on its aerodynamic forces. *Applied Mathematics and Mechanics*, 29(6):731–743, 2008.

[5] C. P. Ellington. The aerodynamics of hovering insect flight. iii. kinematics. *Philosophical Transactions of the Royal Society B: Biological Sciences*, 305(1122):41–78, 1984.

[6] S. M. Walker, A. L. R. Thomas, and G. K. Taylor. Deformable wing kinematics in free-flying hoverflies. *J. R. Soc. Interface*, 7(42):131–142, 2010.

[7] M. Perçin, B. W. van Oudheusden, G. C. H. E. De Croon, and B. Remes. Force generation and wing deformation characteristics of a flapping-wing micro air vehicle 'delfly ii' in hovering flight. *Bioinspiration & Biomimetics*, 11(3):036014, 2016.

[8] G. De Croon, M. Perçin, B. Remes, R. Ruijsink, and C. De Wagter. *The DelFly: Design, Aerodynamics, and Artificial Intelligence of a Flapping Wing Robot*. Springer Netherlands, Dordrecht, 2016.

[9] M. Karasek, A. J. Koopmans, S. F. Armanini, B. D. Remes, and G. C. De Croon. Free flight force estimation of a 23.5 g flapping wing mav using an on-board imu. *Proceedings of the 2016 IEEE/RSJ International Conference on Intelligent Robots and Systems (IROS)*, pages 4963–4969, 2016.

[10] M. Percin, B. W. van Oudheusden, H. E. Eisma, and B. D. W. Remes. Three-dimensional vortex wake structure of a flapping-wing micro aerial vehicle in forward flight configuration. *Experiments in Fluids*, 55(9):729, 2014.

[11] A. del Estal Herrero, M. Percin, M. Karasek, and B. van Oudheusden. Flow visualization around a flapping-wing micro air vehicle in free flight using large-scale piv. *Aerospace*, 5(4):99, 2018.

[12] B. Martínez Gallar, B. W. van Oudheusden, A. Sciacchitano, and M. Karásek. Large-scale flow visualization of a flapping-wing micro air vehicle. *Proceedings 18th International Symposium on Flow Visualization*, 2018.

[13] T. Nakata, H. Liu, Y. Tanaka, N. Nishihashi, X. Wang, and A. Sato. Aerodynamics of a bio-inspired flexible flapping-wing micro air vehicle. *Bioinspiration & Biomimetics*, 6(4):045002, 2011.

[14] P. Wu, B. Stanford, W. Bowman, A. Schwartz, and P. Ifju. Digital image correlation techniques for full–field displacement measurements of micro air vehicle flapping wings. *Experimental Techniques*, 3:53–58, 2009.

[15] D. Song, H. Wang, L. Zeng, and C. Yin. Measuring the camber deformation of a dragonfly wing using projected comb fringe. *Review of Scientific Instruments*, 72(5):2450–2454, 2001.

[16] B. Li and S. Zhang. Superfast high-resolution absolute 3d recovery of a stabilized flapping flight process. *Optics Express*, 25(22):27270–27282, 2017.

[17] H. K. Yuen, J. Princen, J. Illingworth, and J. Kittler. Comparative study of hough transform methods for circle finding. *Image and Vision Computing*, 8(1):71–77, 1990.

[18] S. M. Walker, A. L. R. Thomas, and G. K. Taylor. Photogrammetric reconstruction of high-resolution surface topographies and deformable wing kinematics of tethered locusts and free-flying hoverflies. *J. R. Soc. Interface*, 6:351–366, 2009.

[19] S. Deng. *Aerodynamics of Flapping-wing Micro-Air-Vehicle*. PhD thesis, Technische Universiteit Delft, Delft, 2016.

[20] M. Karásek, F. T. Muijres, C. De Wagter, B. D. W. Remes, and G. C. H. E. De Croon. A tailless aerial robotic flapper reveals that flies use torque coupling in rapid banked turns. *Science*, 361(6407):1089–1094, 2018.